High-Throughput Correlative Electrochemistry−Microscopy at a Transmission Electron Microscopy (TEM) Grid Electrode

Isabel M. Ornelas,[†] Patrick R. Unwin[‡,*] and Cameron L. Bentley[‡,*]

[†]Nanoscale Physics, Chemistry and Engineering Research Laboratory, University of Birmingham, Birmingham B15 2TT, U.K.

[‡]Department of Chemistry, University of Warwick, Coventry CV4 7AL, U.K.

ABSTRACT: As part of the revolution in electrochemical nanoscience, there is growing interest in using electrochemistry to create nanostructured materials, and to assess properties at the nanoscale. Herein, we present a platform that combines scanning electrochemical cell microscopy with *ex-situ* scanning transmission electron microscopy, to allow the ready creation of an array of nanostructures coupled with atomic-scale analysis. As an illustrative example, we explore the electrodeposition of Pt at carbon-coated transmission electron microscopy (TEM) grid supports, where in a single high-throughput experiment it is shown that Pt nanoparticle (PtNP) density increases and size polydispersity decreases with increasing overpotential (*i.e.*, driving force). Furthermore, the coexistence of a range of nanostructures − from single atoms to aggregates of crystalline PtNPs − during the early stages of electrochemical nucleation and growth supports a non-classical *aggregative growth mechanism*. Beyond this exemplary system, the presented correlative electrochemistry−microscopy approach is generally applicable to solve the ubiquitous structure-function problems in electrochemical science and beyond, positioning it as a powerful platform for the rational design of functional nanomaterials.

Over the past three decades, science has been impacted massively by the revolution in nanotechnology. For example, nanoparticles (NPs) have found a plethora of technical applications, including in (electro)catalysis, sensing, spectroscopy, and (bio)medicine.[1-2] NPs are known to possess strongly structure-dependent reactivity, meaning that at the single-NP level there can be large functional differences between even superficially similar NPs due to minute variations in size, surface faceting, defects *etc*.[2-3] For this reason, there is a need for techniques capable of producing single NPs and screening their properties at the *single-entity* level.[4-6]

Scanning electrochemical cell microscopy (SECCM)[7] is a powerful tool in *single-entity* studies, in which the meniscus cell protruding from an electrolyte-filled micropipet (or nanopipet) probe is used to electrochemically interrogate a single or small population of supported NPs within an ensemble.[4, 8-11] For example, in a recent study, SECCM was deployed as a high-throughput screening method to probe the heterogeneous response of individual $LiMn_2O_4$ particles (a Li-ion battery cathode material), revealing a diverse library of responses within a family of superficially similar *single-entities*.[12] The meniscus cell configuration of SECCM also enables local decoration (*i.e.*, micro- or nano-fabrication) at electrodes surfaces, *e.g.*, with metal NPs,[13-14] polymer nanostructures[15] and graphene microwires.[16] Here, we present a platform whereby PtNP "micro-ensembles" are locally electrodeposited under a series of different (tunable) conditions and subsequently characterized *ex-situ* with aberration-corrected high-angle annular dark-field scanning transmission electron microscopy (HAADF-STEM), allowing the relationship between applied potential (E_{app}) and Pt deposit morphology (*i.e.*, NP size, shape and density) to be studied in a detailed high-throughput manner.

Pt plays an essential role as a catalyst in many industrial applications and green energy technology (*e.g.*, autocatalysts and fuel cells). Due its high cost and scarcity, considerable research efforts have focused on developing catalysts with high mass-specific activities (*i.e.*, low Pt loadings), usually achieved by engineering Pt-based nanomaterials with optimal surface-specific activities and high surface-area-to-volume ratios.[17] Among a range of synthetic approaches,[2] electrodeposition is attractive for producing PtNP electrocatalysts, as it generates particles that grow directly on the conductive support to ensure good electrical contact; can be performed with simple equipment under (near) ambient conditions; is scalable and; is relatively low-cost. Tuning of experimental parameters (*e.g.*, E_{app}) offers some control over NP morphology,[18] however, achieving a narrow size distribution is still a challenge,[19] at least partly due to an incomplete mechanistic (atomistic) understanding of the early stages of electrochemical nucleation and growth.[20]

Classical models of nucleation and growth describe immobile nuclei that need to reach a certain critical size to become stable on a low-energy support, which then grow radially by direct addition of atoms through electroreduction (*i.e.*, Volmer−Weber 3D island growth).[21] Recently, through the use of various techniques, including HAADF-STEM,[20, 22-24] ultramicroelectrodes[25] and SECCM[13-14] a more complex *electrochemical aggregative growth mechanism* has been proposed to explain the earliest stages of nucleation and growth,[20] where the formation, aggregation and coalescence of discrete NPs are initially the dominant processes driving the formation of stable structures during electrodeposition. The details of this generalized model are still under discussion,[26] but it has been applied to a number of metal systems,[13-14, 24] including Pt,[23] which undergoes a relatively complex electrodeposition process due to sluggish nucleation/growth kinetics and competing electrochemical processes (*e.g.*, hydrogen evolution reaction, HER). Here, we investigate this complex system to demonstrate the great versatility and strength of a high-throughput electrochemistry−microscopy platform, which enables Pt deposition to be probed with single-atom sensitivity for a range of different conditions in each single experiment, providing a wealth of experimental data.

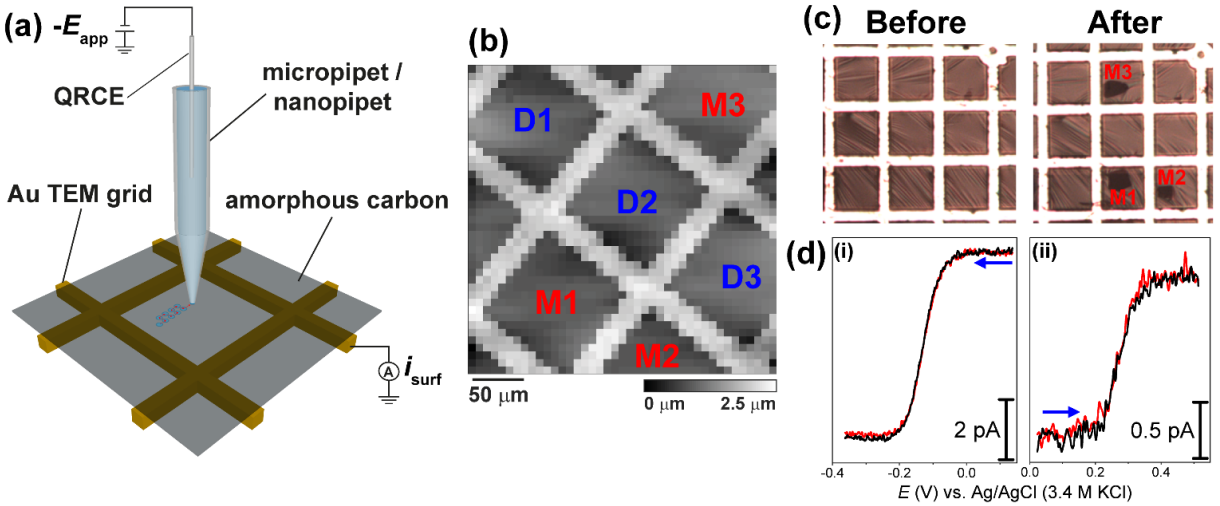

Figure 1. (a) Schematic showing the operation of hopping-mode SECCM. A single channel micropipet probe is employed to make local electrochemical measurements at a CCTG, by applying a potential ($-E_{app}$) at the QRCE in the probe and measuring the current at the surface (i_{surf}). **(b)** Topographical map of a CCTG obtained *in-situ* with SECCM, using a basic hopping mode protocol (see SI, Section S1). **(c)** Optical micrographs of a CCTG taken before and after an SECCM experiment. **(d)** Steady-state voltammograms obtained at CCTG (black trace) and Au (red trace) substrates, showing the **(i)** reduction of 4 mM $[Ru(NH_3)_6]^{3+}$ (100 mM KCl) and **(ii)** oxidation of 1 mM FcDM (33 mM KCl). The LSVs were obtained in the SECCM configuration with a nanopipet probe of diameter ≈150 nm and $\upsilon = 0.1$ V s^{-1}.

EXPERIMENTAL SECTION

Details on the chemical reagents and electrode materials; electrochemical measurements; STEM imaging and; data processing and analysis procedures, are included in the Supporting Information (SI), Section S1. SECCM was performed on a home-built scanning electrochemical probe microscopy workstation,[27-28] detailed in Section S1 and shown schematically in Figure 1a. During operation, a micropipet (or nanopipet) probe filled with electrolyte solution and equipped with a quasi-reference counter electrode (QRCE), was used to perform local electrochemistry on a carbon-coated Au TEM grid (CCTG) working electrode. To facilitate the straightforward use of environmental control (*vide infra*), and subsequent microscopy analysis, probe positioning was achieved through *in-situ* topographical mapping, as shown in Figure 1b.

After topographical mapping, electrochemistry (*e.g.*, electrodeposition) was performed on the free-standing carbon areas of the CCTG. The micropipet probe was of diameter 1.6 μm (Figure S1) and filled with a solution of $K_2[PtCl_4]$ (Pt precursor salt, 1 mM) and HCl (supporting electrolyte, 100 mM). A Pt wire inserted into the back of the micropipet served as a QRCE, meaning all potentials are referenced to the Pt(II)/Pt(0) process (measured to have a stable potential of 0.55 ± 0.01 V vs. Ag/AgCl, 3.4 M KCl) and can thus be directly related to overpotential (η). Oxygen (O_2) was excluded from the SECCM droplet cell through the use of an argon-purged environmental cell, the designs of which are included in the SI, Section S2.

Following electrochemistry, the CCTG was "marked" by pushing the micropipet tip through the carbon film in adjacent unused squares (M1 – M3, Figure 1b) to make holes, shown in Figure 1c. The marked areas of the CCTG were used as a guide to locate the PtNP microensembles (D1 − D3, Figure 1b) for *ex-situ* STEM imaging. HAADF-STEM images were recorded at 200 kV using a Cs aberration corrected (CEOS, Germany) JEM-2100F field emission electron microscope (JEOL, Japan), employing inner and outer collection angles of 62 and 164 mrad, respectively, a convergence angle of 19 mrad, and a pixel dwell time of 38 μs (10.0 s per image, 512 × 512 pixels).

RESULTS AND DISCUSSION

Local electrochemistry on a TEM grid electrode. Prior to use as a support electrode for electrodeposition, the performance of the CCTG as a general electrode was benchmarked by investigating two rapid, mechanistically simple outer-sphere electron transfer processes: $[Ru(NH_3)_6]^{2+/3+}$ and $FcDM^{0/+}$ (where FcDM = 1,1′-ferrocenedimethanol),[29] shown in Figure 1d. Due to the conical geometry of the pipet probes used in SECCM, mass-transport is predominantly governed by (quasi-)radial diffusion, allowing (near) steady-state conditions to be established on the ms timescale (scan rate, $\upsilon < 1$ V s^{-1}).[27, 30] Thus, the voltammograms in Figure 1d are sigmoidal-shaped, with a mass-transport limited current (i_{lim}) that is *ca.* 10% of that expected at a conventional inlaid disc electrode of the same diameter as the used nanopipet probe (*ca.* 150 nm).[27] The steady-state voltammograms measured on the CCTG (black curves) are indistinguishable from those from a conventional metal (Au) electrode (red curves), and satisfy Tomes criterion of reversibility (*i.e.*, $|E_{3/4} - E_{1/4}| \approx 56$ mV, where $E_{3/4}$ and $E_{1/4}$ are the quarter- and three quarter-wave potentials, respectively).[29] This confirms that the free-standing carbon areas of the CCTGs are able to support rapid electron-transfer within the E_{app} range explored during Pt electrodeposition [*i.e.*, *ca.* −0.05 to −0.95 V vs. Pt(II)/Pt(0)].

Pt electrodeposition: cyclic voltammetry. Pt electrodeposition on a CCTG was initially investigated using cyclic voltammetry in the SECCM configuration. Shown in Figure 2a, the cyclic voltammograms (CVs) exhibit a non-classical shape expected for nucleation and growth on a low-energy substrate (*i.e.*, CCTG), with no discernible reduction processes observed until $E_{app} \approx -0.6$ V vs. Pt(II)/Pt(0), where the onset of HER occurs. Noted above, the mass-transport limited current density (j_{lim}) for a diffusion-controlled process in SECCM is *ca.* 10% of that for the same-sized microdisk electrode (≈2 μm), which for a 2e$^-$ process corresponds to *ca.* −3 mA cm^{-2} ($i_{lim} = -60$ pA, detailed in the SI, Section S3). Evidently, no such process is observed, however the occurrence of the HER at $E_{app} \approx 0$ V vs. RHE (reversible hydrogen electrode) and the increase in j_{HER} with cycling are both indicators that Pt is in fact deposited. Thus, it is

clear that the Pt(II)/Pt(0) process is not mass-transport controlled, but rather kinetically-limited on the CCTG support.[20]

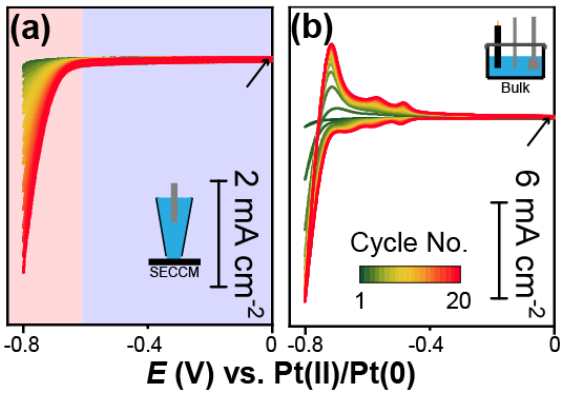

Figure 2. CVs (20 cycles) obtained from a solution of 1 mM $K_2[PtCl_4]$ and 100 mM HCl, with υ = 0.5 V s^{-1}. Red ($E_{app} \leq -0.6$ V) and blue ($E_{app} > -0.6$ V) indicate potentials where the HER does and does not occur, respectively. **(a)** was carried out in the SECCM configuration with a 1.6 µm diameter micropipet probe at a CCTG electrode and **(b)** was carried out in bulk (*i.e.*, the macroscale) at a GC electrode (electrode area, A = 0.707 cm^2). Note the differing j scales. The arrows indicate 0 mA cm^{-2}.

As a point of comparison, the Pt(II)/Pt(0) process was further investigated in a conventional 3-electrode format on a glassy carbon (GC) macroelectrode, which is a widely used low energy carbon material in bulk electrochemistry and electrodeposition experiments.[29] Shown in Figure 2b, a similar pattern of reactivity is observed at the GC substrate, with relatively small j values initially measured (cycle 1) that grow continuously with potential cycling. Interestingly, j increases with cycling at a much faster rate on GC compared to CCTG suggesting that the kinetics of Pt nucleation is slower on the latter support, giving rise to a significant time lag during electrodeposition. Thus, comparatively more Pt is deposited during potential cycling on GC, resulting in a larger active (Pt) surface area and the appearance of the additional processes of hydrogen adsorption/desorption (symmetrical peaks at *ca.* −0.49 and −0.58 V) and Pt deposition onto Pt[20, 22-23] (reductive peak at *ca.* −0.67 V). Note that these processes also occur during potential cycling on CCTGs in the SECCM configuration (Figure 2a), but do not give rise to discernible reduction currents in the CV due to the comparatively small deposited surface area of Pt on this timescale (*i.e.*, the processes cannot be distinguished from the nonfaradaic baseline current, analogous to cycles 1 – 5 on GC, Figure 2b). Overall, the CCTG and GC supports behave analogously as supports for Pt electrodeposition, albeit with a significant time lag (*i.e.*, slower kinetics) at the former compared to the latter.

Pt electrodeposition: chronoamperometry. Pt electrodeposition was further explored using chronoamperometry, where a series of depositions were carried out on the CCTG electrode by varying E_{app} from 0 to −0.9 V vs. Pt(II)/Pt(0) in 0.1 V increments. It is worth reemphasizing that this approach is: (i) high-throughput, *i.e.*, a range of deposition parameters (E_{app} and/or deposition time) can be explored in a single experiment; (ii) high-resolution, *i.e.*, the use of a CCTG support enables complementary, co-located structural analysis through STEM with single-atom sensitivity[24] and; (iii) statistically sound, *i.e.*, each individual NP within the microensemble can be counted and characterized. Importantly, although it has been exclusively applied to study electrodeposition herein, this approach would be applicable to any class of material that can be studied by (S)TEM (*e.g.*, supported NPs, thin films *etc.*).

Chronoamperograms (CAs) obtained in the SECCM configuration on a CCTG are shown in Figure 3a. In general, $|j|$: increases with decreasing E_{app} (increasing η); decays towards zero at $E_{app} \geq -0.6$ V and; increases with time at $E_{app} < -0.6$ V. The increasing $|j|$ at $E_{app} < -0.6$ V is attributed to the HER [the contribution of Pt(II)/Pt(0) to j is negligible, see Figure 2], which plateaus at longer times, shown in Figure 3b, implying that the active surface area of the deposited Pt initially grows before reaching a stable value. In other words, as the HER is predominantly surface-controlled at $E_{app} \leq -0.9$ V, j directly indicates the Pt surface area, which reaches a constant value after *ca.* 4 seconds. Shown in Figure 3c, the charge passed during reduction (Q) increases with decreasing E_{app} (increasing η), consistent with Figure 3b and c. In the absence of the competing HER (*i.e.*, $E_{app} \geq -0.6$ V), Q is a direct measure of the amount of Pt deposited (Figure 3e, inset), which exhibits a relatively weak dependence on E_{app} (*i.e.*, Q only increased *ca.* 18-fold from η = 0.1 to 0.6 V). Note that repeat experiments carried out in adjacent squares confirm that the Pt electrodeposition process was consistent across the CCTG surface, shown in the SI, Section S4.

Again, as a point of comparison, analogous experiments were carried out in a conventional 3-electrode format on a GC macroelectrode, shown in Figure 3d. The aforementioned time lag during Pt electrodeposition at CCTGs compared to GC is clear when comparing Figure 3a and d, where at E_{app} = −0.8 and −0.9 V, $|j|$ is *ca.* one order-of-magnitude lower at the former compared to the latter. At longer times, the CAs obtained at GC (Figure 3e) and CCTGs (Figure 3b) display very similar characteristics (*i.e.*, morphology and j), indicating that while the initial nucleation process(es) are more sluggish on the CCTGs, the growth processes are largely unaffected by the identity of the low energy carbon support.

Classical 3D island growth models of electrodeposition predict a steady increase in the Pt surface area with time, contrary to the results presented in Figure 3b and e. One possible explanation for the constant active surface area would be that Pt electrodeposition completely ceases after *ca.* 4 seconds. While adsorbed H (H_{ads}) has been shown to the limit growth of Pt on Pt (termed self-terminating growth),[31] this cannot explain inhibition of Pt nucleation on the CCTG (or GC) support itself, and further is inconsistent with our observation of 3D Pt nanostructures (*vide infra*). In addition, physical blockage of nucleation sites (on the CCTG) by H_2 nanobubbles generated during the HER is also unlikely at pH > 0, due to fast gas-exchange across the gas-liquid interface in the SECCM configuration.[32] Another possible explanation is that the formation of Pt through nucleation and growth proceeds in parallel with aggregative growth processes[20, 23] that effectively annihilate Pt surface area. In this scenario, nucleation and growth processes would initially dominate at t < 4 s, before being eventually balanced by aggregative processes leading to coalescence, giving rise to a relatively constant active surface area at t > 4 s. Indeed, the existence of parallel classical nucleation/growth and aggregative growth pathways is supported by our STEM observations, below.

Correlative STEM analysis. Following the electrodeposition experiments (Figure 3), the Pt "microensembles" on the CCTG substrate were imaged *ex-situ* with HAADF-STEM, which is a powerful tool for analyzing structures arising from nucleation and growth due to its large dynamic magnification range that enables visualization of the whole droplet footprint (commensurate with the size of the micropipet probe, shown in the SI,

Section S5) and down to single atoms with sub-nanometer resolution.[24] We demonstrate this herein by considering the E_{app}-dependent NP distributions (*i.e.*, size, particle count and Pt mass) and NP morphologies. Note that only PtNP microensembles obtained at $E_{app} \leq -0.6$ V have been analyzed in detail (at $E_{app} > -0.6$ V, the PtNPs were too small and/or too few to be resolved at a low magnification, Figure S7). Particle size analysis was performed on low magnification images (Figure 4a-d), with the resulting distributions given in Figure 4e (further details can be found in the SI, Section S6). For all E_{app}, the histograms comprise bimodal distributions (also reflected in the N histograms, SI, Figure S9), with a sharp peak at very small NP sizes (<2 nm), and a broader wave for larger NP sizes, consistent with the literature.[20]

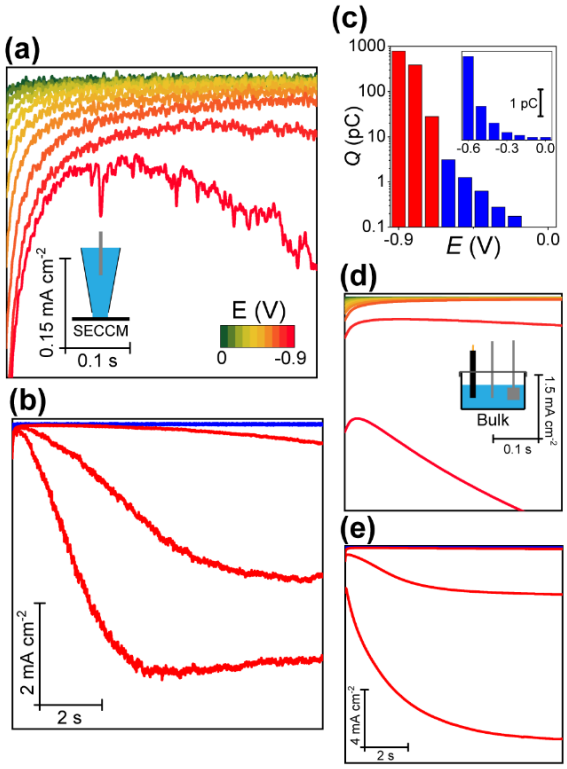

Figure 3. CAs obtained in the SECCM configuration at a CCTG, with E_{app} = 0 to −0.9 V (0.1 V increments). **(a)** First 0.5 s and **(b)** full 10 s of the transient. **(c)** Bar chart showing the charge (Q) passed during each i−t transient in (b) versus E_{app}. Note the logarithmic scale. Inset is a plot showing only $E_{app} \geq -0.6$ V vs. Pt(II)/Pt(0), where Pt electrodeposition is the dominant process, plotted on a linear scale. **(d)** and **(e)** are analogous to (a) and (b), respectively, except carried out in bulk at a GC macroelectrode. Note the differing current and time scales.

The SECCM microensembles provide a wealth of information on how NP size distributions are affected by deposition parameters. In general, the percentage of small NPs ($d \leq 2$ nm) decreases with increasing η, while the percentage of medium-sized NPs ($2 < d < 8$ nm) increases. In addition, the percentage of large NPs ($d > 10$ nm) decreases with increasing driving force, as does the maximum diameter of the NPs (*ca.* 13 and 21 nm at $E_{app} = -0.9$ and −0.6 V, respectively). For the largest driving forces, $E_{app} = -0.8$ and −0.9 V, the histograms are very similar, indicating that the deposition mechanism does not change within this potential range (consistent with the electrochemical data, Figure 3). Low magnification images also show that the particle density and total amount of Pt increase with $E_{app} = -0.6$ V to −0.8 V, and less strongly from −0.8 V to −0.9 V. A particle count and estimation of the total platinum mass (the methodology is described in the SI, Section S6) confirm this trend, as summarized in Table S1. Alluded to above, a narrow (and ideally controllable) NP size distribution is preferable from a practical standpoint,[2] which, from this SECCM experiment is shown to be very sensitive to E_{app}, with larger η (and possibly hydrogen coevolution[33]) giving rise to a more narrow size distributions (*i.e.*, smaller size polydispersity). Other experimental parameters that could be systematically explored in this high-throughput configuration include the deposition time and/or deposition waveform (*e.g.*, designer E−t waveforms[18]).

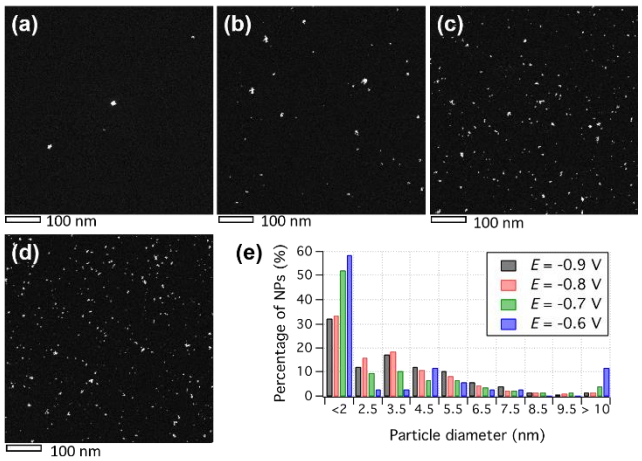

Figure 4. Representative low magnification (250k) STEM images of Pt electrodeposited at E_{app} = **(a)** −0.6 V, **(b)** −0.7 V, **(c)** −0.8 V, **(d)** −0.9 V, all at 10 s deposition time. **(e)** Particle diameter distributions (histograms).

Figure 5 shows high magnification images of representative PtNPs morphologies at 3 different potentials where parallel HER is and is not important, which we use to gain an atomistic view of electrochemical nucleation and growth.[20, 22, 24] Generally, the smallest clusters do not have a well-defined structure (*e.g.*, cluster 1 in Figure 5a; note the inset FFT, which indicates that the cluster is amorphous). For clusters with diameters larger than ≈2 nm, the structure becomes monocrystalline (*e.g.*, cluster 2 in Figure 5a, and the smallest cluster in Figure 5b), and above ≈4 nm, one or more grain boundaries can be identified within the same particle (Figure 5b-d). From this, we infer that clusters are initially formed by a direct addition mechanism (*i.e.*, addition of single atoms) up to a critical size, and larger particles must be formed by the aggregation of these smaller clusters, in agreement with the generalized *electrochemical aggregative growth mechanism*.[20, 23]

It is also important to note that, independently of E_{app} *and the size of and distance to the nearest NP*, single Pt atoms were seen consistently across the CCTG (indicated by red arrows in Figure 5). From the spatial distribution of these single atoms, it is unlikely that they were ejected from neighboring NPs due to electron beam exposure (explored in the SI, Section S7), but rather must originate from the Pt electrodeposition process. There is significant interest in stable single atoms for use in applications such as (electro)catalysis,[34] but the role of these entities in the early stages of electrochemical nucleation and growth is still debated, although recent studies have provided indirect (through voltammetry[25]) or direct (through *ex-situ* STEM imaging[24]) evidence for their existence. In any case, the coexistence of single atoms (Figure 5a-d) and amorphous (Figure 5a),

monocrystalline (Figure 5a-b) and polycrystalline (Figure 5b-d) NPs (and aggregates of these), indicates that several early growth mechanisms occur simultaneously.[20]

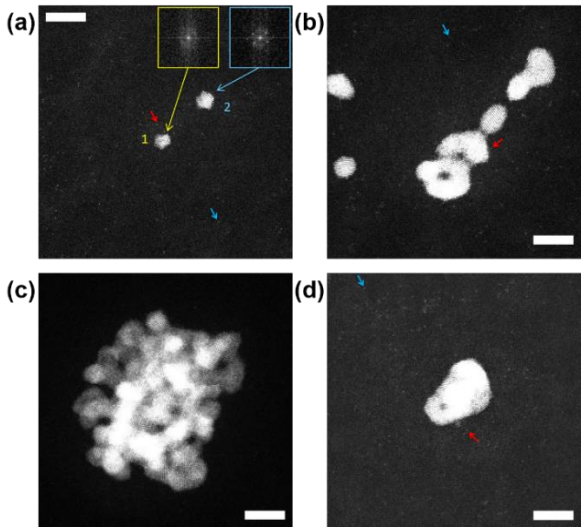

Figure 5. High magnification (5M) HAADF-STEM images of PtNPs deposited at **(a - b)** E_{app} = −0.9 V, **(c)** E_{app} = −0.6 V, and **(d)** E_{app} = −0.5 V. Insets in (a) are FFTs obtained from the highlighted NPs. The scale bars indicate 5 nm in all images. The red and blue arrows in (a), (b) and (d) indicate single Pt atoms located near (<2 nm) and far from the featured NPs, respectively.

CONCLUSIONS

In conclusion, we have presented a high-throughput SECCM-STEM platform that allows structure-electrochemistry to be correlated with single-atom sensitivity. Applied to Pt electrodeposition on a CCTG as an exemplary system, in a single experiment, it was shown that PtNP density increases and size polydispersity decreases with increasing driving force (*i.e.*, increasing η). Furthermore, it was shown that structures ranging from single Pt atoms (imaged directly on the CCTG support) to amorphous, monocrystalline and polycrystalline PtNPs (and aggregates of these) coexist during the early stages of nucleation and growth, further supporting the existence of an electrochemical aggregative growth mechanism.[20] Beyond this system, the presented *correlative electrochemistry−microscopy* approach should be generally applicable to any class of (electro)material, for example battery materials[12] and electrocatalysts,[9] positioning this technology as a powerful tool for structure-property elucidation and the rational design of functional materials.

ASSOCIATED CONTENT

Supporting Information

Experimental section (Section S1); details on the environmental cell (S2); calculation of i_{lim} in the SECCM configuration (S3); repeat SECCM experiments (S4); low-magnification images of the Pt microensembles (S5); quantifying Pt through HAADF-STEM intensity (S6) and; effect of beam exposure on single Pt atoms (S7).

AUTHOR INFORMATION

Corresponding Author

* P.R.Unwin@warwick.ac.uk (P.R.U.); C.Bentley.1@warwick.ac.uk (C.L.B.)

ACKNOWLEDGMENT

The STEM instrument was obtained through the Birmingham Science City project "Creating and Characterizing Next Generation Advanced Materials", supported by Advantage West Midlands and partially funded by the European Regional Development Fund. P.R.U. gratefully acknowledges support from a Royal Society Wolfson Research Merit Award and EPSRC (EP/R018820/1). C.L.B. acknowledges financial support from the Ramsay Memorial Fellowship Trust. The authors acknowledge Prof D. M. Haddleton for helpful suggestions on the design of the environmental cell.

REFERENCES

1. Burda, C.; Chen, X.; Narayanan, R.; El-Sayed, M. A., Chemistry and Properties of Nanocrystals of Different Shapes. *Chem. Rev.* **2005**, *105*, 1025-1102.
2. Kleijn, S. E. F.; Lai, S. C. S.; Koper, M. T. M.; Unwin, P. R., Electrochemistry of Nanoparticles. *Angew. Chem.-Int. Edit.* **2014**, *53*, 3558-3586.
3. Koper, M. T. M., Structure Sensitivity and Nanoscale Effects in Electrocatalysis. *Nanoscale* **2011**, *3*, 2054-2073.
4. Bentley, C. L.; Kang, M.; Unwin, P. R., Nanoscale Surface Structure-Activity in Electrochemistry and Electrocatalysis. *J. Am. Chem. Soc.* **2019**, *141*, 2179-2193.
5. Baker, L. A., Perspective and Prospectus on Single-Entity Electrochemistry. *J. Am. Chem. Soc.* **2018**, *140*, 15549-15559.
6. Crooks, R. M., Concluding Remarks: Single Entity Electrochemistry one step at a time. *Faraday Discuss.* **2016**, *193*, 533-547.
7. Bentley, C. L.; Kang, M.; Unwin, P. R., Scanning Electrochemical Cell Microscopy: New Perspectives on Electrode Processes in Action. *Curr. Opin. Electrochem.* **2017**, *6*, 23-30.
8. Ustarroz, J.; Ornelas, I. M.; Zhang, G.; Perry, D.; Kang, M.; Bentley, C. L.; Walker, M.; Unwin, P. R., Mobility and Poisoning of Mass-Selected Platinum Nanoclusters during the Oxygen Reduction Reaction. *ACS Catal.* **2018**, *8*, 6775-6790.
9. Tarnev, T.; Barike Aiyappa, H.; Botz, A.; Erichsen, T.; Ernst, A.; Andronescu, C.; Schuhmann, W., SECCM Investigation of Single ZIF-Derived Nanocomposite Particles as Oxygen Evolution Electrocatalysts in Alkaline Media. *Angew. Chem.-Int. Edit.* **2019**, *58*, 14265-14269.
10. Saha, P.; Hill, J. W.; Walmsley, J. D.; Hill, C. M., Probing Electrocatalysis at Individual Au Nanorods via Correlated Optical and Electrochemical Measurements. *Anal. Chem.* **2018**, *90*, 12832-12839.
11. Lai, S. C. S.; Dudin, P. V.; Macpherson, J. V.; Unwin, P. R., Visualizing Zeptomole (Electro)Catalysis at Single Nanoparticles within an Ensemble. *J. Am. Chem. Soc.* **2011**, *133*, 10744-10747.
12. Tao, B.; Yule, L. C.; Daviddi, E.; Bentley, C. L.; Unwin, P. R., Correlative Electrochemistry-Microscopy of Li-ion (De)intercalation at Series of Individual $LiMn_2O_4$ Particles. *Angew. Chem.-Int. Edit.* **2019**, *58*, 4606-4611.
13. Lai, S. C. S.; Lazenby, R. A.; Kirkman, P. M.; Unwin, P. R., Nucleation, Aggregative Growth and Detachment of Metal Nanoparticles during Electrodeposition at Electrode Surfaces. *Chem. Sci.* **2015**, *6*, 1126-1138.
14. Kim, Y. R.; Lai, S. C. S.; McKelvey, K.; Zhang, G. H.; Perry, D.; Miller, T. S.; Unwin, P. R., Nucleation and Aggregative Growth of Palladium Nanoparticles on Carbon Electrodes: Experiment and Kinetic Model. *J. Phys. Chem. C* **2015**, *119*, 17389-17397.
15. McKelvey, K.; O'Connell, M. A.; Unwin, P. R., Meniscus Confined Fabrication of Multidimensional Conducting Polymer Nanostructures with Scanning Electrochemical Cell Microscopy (SECCM). *Chem. Commun.* **2013**, *49*, 2986-2988.
16. Chang, W. S.; Jeong, H.; Kim, J. H.; Lee, S.; Wajahat, M.; Han, J. T.; Cho, S. H.; Seol, S. K., Micropatterning of Reduced Graphene Oxide by Meniscus-Guided Printing. *Carbon* **2017**, *123*, 364-370.
17. *Electrocatalysis in Fuel Cells: A Non and Low Platinum Approach*; Springer: New York, 2013.
18. Tian, N.; Zhou, Z.-Y.; Sun, S.-G.; Ding, Y.; Wang, Z. L., Synthesis of Tetrahexahedral Platinum Nanocrystals with High-Index Facets and High Electro-Oxidation Activity. *Science* **2007**, *316*, 732-735.
19. Penner, R. M., Mesoscopic Metal Particles and Wires by Electrodeposition. *J. Phys. Chem. B* **2002**, *106*, 3339-3353.

20. Ustarroz, J.; Hammons, J. A.; Altantzis, T.; Hubin, A.; Bals, S.; Terryn, H., A Generalized Electrochemical Aggregative Growth Mechanism. *J. Am. Chem. Soc.* **2013**, *135*, 11550-11561.
21. Budevski, E.; Staikov, G.; Lorenz, W. J., *Electrochemical Phase Formation and Growth*; Wiley-VCH: Weinheim, Germany, 1996, p 410.
22. Ustarroz, J.; Gupta, U.; Hubin, A.; Bals, S.; Terryn, H., Electrodeposition of Ag Nanoparticles onto Carbon Coated TEM Grids: A Direct Approach to Study Early Stages of Nucleation. *Electrochem. Comm.* **2010**, *12*, 1706-1709.
23. Ustarroz, J.; Altantzis, T.; Hammons, J. A.; Hubin, A.; Bals, S.; Terryn, H., The Role of Nanocluster Aggregation, Coalescence, and Recrystallization in the Electrochemical Deposition of Platinum Nanostructures. *Chem. Mat.* **2014**, *26*, 2396-2406.
24. Hussein, H. E. M.; Maurer, R. J.; Amari, H.; Peters, J. J. P.; Meng, L.; Beanland, R.; Newton, M. E.; Macpherson, J. V., Tracking Metal Electrodeposition Dynamics from Nucleation and Growth of a Single Atom to a Crystalline Nanoparticle. *ACS Nano* **2018**, *12*, 7388-7396.
25. Zhou, M.; Bao, S.; Bard, A. J., Probing Size and Substrate Effects on the Hydrogen Evolution Reaction by Single Isolated Pt Atoms, Atomic Clusters, and Nanoparticles. *J. Am. Chem. Soc.* **2019**, *141*, 7327-7332.
26. Mamme, M. H.; Köhn, C.; Deconinck, J.; Ustarroz, J., Numerical Insights into the Early Stages of Nanoscale Electrodeposition: Nanocluster Surface Diffusion and Aggregative Growth. *Nanoscale* **2018**, *10*, 7194-7209.
27. Snowden, M. E.; Güell, A. G.; Lai, S. C. S.; McKelvey, K.; Ebejer, N.; O'Connell, M. A.; Colburn, A. W.; Unwin, P. R., Scanning Electrochemical Cell Microscopy: Theory and Experiment for Quantitative High Resolution Spatially-Resolved Voltammetry and Simultaneous Ion-Conductance Measurements. *Anal. Chem.* **2012**, *84*, 2483-2491.
28. Ebejer, N.; Güell, A. G.; Lai, S. C. S.; McKelvey, K.; Snowden, M. E.; Unwin, P. R., Scanning Electrochemical Cell Microscopy: A Versatile Technique for Nanoscale Electrochemistry and Functional Imaging. In *Annual Review of Analytical Chemistry, Vol 6*, Cooks, R. G.; Pemberton, J. E., Eds. Annual Reviews: Palo Alto, 2013; Vol. 6, pp 329-351.
29. Zoski, C. G., *Handbook of Electrochemistry*, 1st ed.; Elsevier: Amsterdam, 2007, p 892.
30. Momotenko, D.; Byers, J. C.; McKelvey, K.; Kang, M.; Unwin, P. R., High-Speed Electrochemical Imaging. *ACS Nano* **2015**, *9*, 8942-8952.
31. Liu, Y. H.; Gokcen, D.; Bertocci, U.; Moffat, T. P., Self-Terminating Growth of Platinum Films by Electrochemical Deposition. *Science* **2012**, *338*, 1327-1330.
32. Wang, Y.; Gordon, E.; Ren, H., Mapping the Nucleation of H_2 Bubbles on Polycrystalline Pt via Scanning Electrochemical Cell Microscopy. *J. Phys. Chem. Lett.* **2019**, *10*, 3887-3892.
33. Zach, M. P.; Penner, R. M., Nanocrystalline Nickel Nanoparticles. *Adv. Mat.* **2000**, *12*, 878-883.
34. Wang, A.; Li, J.; Zhang, T., Heterogeneous single-atom catalysis. *Nat. Rev. Chem.* **2018**, *2*, 65-81.

TOC Graphic:

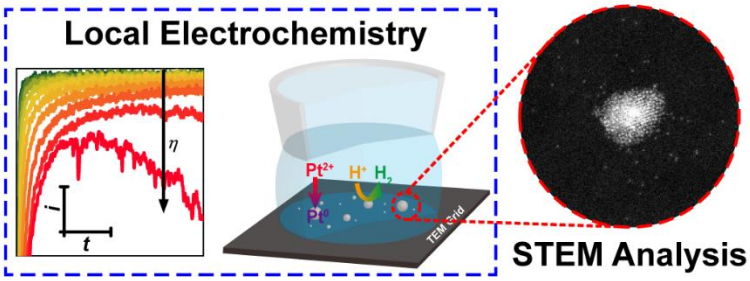
Local Electrochemistry
η
i
t
Pt2+
H+
H2
Pt
TEM Grid
STEM Analysis